(Received 27 March 2026, Accepted 26 April 2026, Scheduled 15 May 2026)

Analysis and Optimization of AMF Contacts in Vacuum Interrupters under Short-Circuit Current Excitation

Siying Yang, Yuan Feng, Zechen Bai, Xuanyu Guan, Shuhong Wang, and Naming Zhang*

School of Electrical Engineering, Xi'an Jiaotong University, Xi'an 710049, China

ABSTRACT: The existing research on axial magnetic field (AMF) contacts in vacuum interrupters mostly focuses on power frequency or low current conditions and lacks in-depth optimization of magnetic field characteristics and contact structure parameters under short-circuit current impact. Therefore, the AMF characteristics of the vacuum interrupter under short-circuit current excitation are studied, and the contact structure parameters are optimized. Firstly, a three-dimensional transient electromagnetic field model of the vacuum interrupter, excited by the measured short-circuit current, is constructed, and the effects of four key geometric parameters — contact slotting angle, cup finger angle, slotting length, and slotting width — on the peak AMF are quantified. Secondly, the orthogonal test method is used to screen significant factors, and it is concluded that cup finger angle is the most critical parameter among the four. Finally, a quadratic regression model is constructed by combining the response surface model (RSM) to explore parameter interactions. The theoretical optimum is obtained and further refined through boundary verification to yield the actual optimal parameter combination. This study guides the design of AMF contacts in vacuum circuit breakers under short-circuit conditions.

1. INTRODUCTION

In recent years, with the continuous expansion of the scale of power grids, the voltage level and loads throughout the entire grid have been continuously increasing [1, 2]. As a key piece of protective equipment, the performance of circuit breakers directly affects the safe and stable operation of the entire power grid [3–5]. Since then, SF_6 gas has been widely used in high-pressure applications owing to its excellent insulation and arc-extinguishing properties. However, its strong greenhouse effect has been a major concern for the international community and has been strictly restricted and phased out [6–9]. This trend, together with environmental regulations, has brought the development of vacuum circuit breakers (VCBs) into sharp focus in the industry [10–14]. Modern electrical equipment requires a greater capacity. As a result, vacuum interrupters are evolving toward higher current, higher voltage, and greater breaking capacity, where insulation performance is critical. Specifically, the dielectric strength under short-circuit conditions determines the overall insulation level of the equipment [15].

Moreover, the insulation capability is closely related to the short-circuit breaking performance, and the distribution of the AMF is a key physical factor. The AMF influences the insulation properties and affects arc extinction. The strength and uniformity of the AMF govern the rotation and diffusion of the vacuum arc and the thermal load distribution on the contact surfaces. These factors help prevent local arc stagnation, reduce contact erosion, and ensure reliable current interruption [16, 17]. As the most critical component of an interrupter, the optimization of the contact structure is essential. A precise AMF design can improve the breaking performance and reliability of vacuum circuit breakers, which is of significant engineering value [18–20].

Because the magnetic field of the contacts is influenced by multiple factors, many researchers have adopted various approaches to optimize different parameters of the contacts, thereby regulating the AMF within the interrupter [21–28].

However, most existing studies focus on the analysis of magnetic field characteristics under power frequency currents, and there are relatively few studies on the characteristics under the excitation of large short-circuit currents. In this study, the measured large short-circuit current waveform was introduced as the excitation to provide guidance for the analysis of magnetic field characteristics under short-circuit conditions.

Therefore, a three-dimensional electromagnetic field model of a vacuum interrupter contact system is established. Based on finite element analysis software, the experimentally measured short-circuit current is applied as the excitation source. Firstly, the independent influence of four key geometric parameters on the AMF distribution is systematically explored. These four parameters are the slotting angle α, cup finger angle β, slotting length L, and slotting width d. Secondly, on this basis, this study proposes a phased optimization method. Thirdly, multi-parameter screening is performed through orthogonal test design to obtain a preliminary excellent parameter combination quickly. Fourthly, the Box-Behnken (BBD) response surface method is used to establish a quadratic regression model; the interaction between different parameters is discussed in depth; and the theoretical optimal solution is obtained through global optimization. Finally, boundary refinement verification was performed for the boundary effect of the theoretical optimal solution, and the actual global optimal parameter combination

* Corresponding author: Naming Zhang (namingzhang@xjtu.edu.cn).

TABLE 1. Structural parameters of the arc interrupter of the vacuum circuit breaker.

Parameter	Value	Parameter	Value
Contact Radius (mm)	53	Number of Slots	6
Contact Segment Thickness (mm)	3	Cup Finger Angle β (°)	100
Arc Height (mm)	20	Slotting Angle α (°)	25
Stationary Rod Length (mm)	150	Slotting Width d (mm)	1
Moving Rod Length (mm)	100	Slotting Length L (mm)	20

TABLE 2. Material parameters of the vacuum circuit breaker interrupter.

Component	Material	Relative Permeability	Electrical Conductivity (S/m)
Arc	——	1	2000
Cup Base	OFC	1	5.8×10^7
Contact Segment	CuCr25	1	2.8×10^7

was determined. This study reveals the influence of the structural parameters of complex contact systems on the AMF of vacuum interrupters. This study provides a clear parameter basis and theoretical guidance for the fine design and multi-parameter collaborative optimization of high-performance contact systems in vacuum interrupters.

2. VACUUM INTERRUPTER MODEL

2.1. Structure of the Vacuum Interrupter

This study investigated the magnetic field of a 31.5 kV vacuum interrupter. The device comprises stationary and moving conductive rods and stationary and moving contacts. Each contact assembly comprised a contact segment and a cup base. The simplified three-dimensional model is shown in Fig. 1.

As shown in the figure, the moving contact system is composed of moving contact piece 1, moving contact cup holder 5, and dynamic conductive rod 4. The static contact system is composed of six static contact head pieces, two static contact cup holders, and three static conductive rods. When the circuit breaker is opened, an arc is generated between the contacts, and high temperature causes the material on the surface of the contact to volatilize. Owing to the special structure of the contact system, when the current passes through, an AMF is generated, which forces the arc to rotate at high speed and spread outward, promoting the condensation of metal vapor. Eventually, as the current crosses zero, and the arc goes out smoothly, the dielectric strength between the contacts quickly recovers. The 3D simulation model of this vacuum interrupter ignores the secondary structures that have little impact on the magnetic field simulation, such as bellows, shields, and support. Some of its structural parameters are listed in Table 1. In the vacuum interrupter, the dynamic and static contacts are oxygen-free copper, and the contact plates are made of CuCr25 material. To simplify the calculation, the arc between the dynamic and static contacts was equivalent to a conductive cylinder. The material parameters of the entire contact model are listed in Table 2 [29].

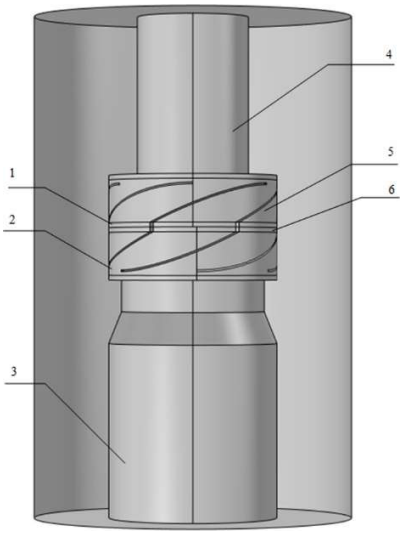

FIGURE 1. Simplified structure of a vacuum interrupter.

2.2. AMF Simulation

A 3D electromagnetic model was established based on the baseline structural parameters listed in Table 1. The short-circuit current enters through the moving contact rod and exits through the stationary contact rod. A measured short-circuit current waveform was applied as the excitation source, with a peak value of 57.7 kA. The current peak occurred at approximately $t = 0.111$ s, whereas the current zero-crossing instant was at $t = 0.1$ s, as shown in Fig. 2.

Figure 3 illustrates the distribution of the AMF within the vacuum interrupter at the times of current zero-crossing and peak current. As shown in Fig. 3, the maximum AMF in the entire vacuum interrupter reached only 7.4×10^{-5} T at the current zero-crossing instant. At this stage, the magnetic field primarily consists of residual magnetism, and its driving effect on the arc is significantly weakened. In contrast, when the short-circuit current reached its peak, the AMF intensity increased substantially, reaching a maximum of 0.301 T. The field is highly concentrated near the slot edges and cup finger roots. Conversely,

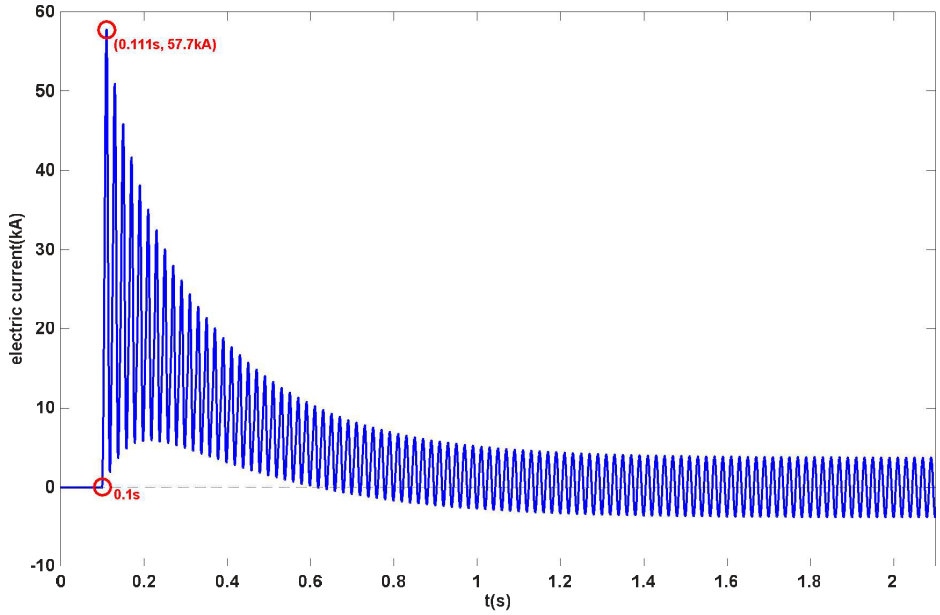

FIGURE 2. Short-circuit current excitation is applied to the vacuum interrupter.

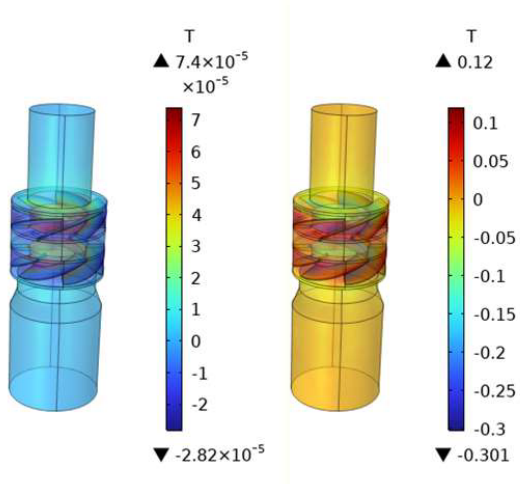

FIGURE 3. AMF distribution in the vacuum interrupter at current zero-crossing and peak current moments.

the longitudinal magnetic field remained relatively weak in the regions of the upper and lower contact rods.

Figure 4 further shows the AMF distribution in the contact area at different moments during the short-circuit process. From the contour plots of the three moments, it can be seen that although the short-circuit current fluctuates constantly, the AMF in the effective breaking area of the contact still maintains a high degree of axial symmetry, and the field strength is always concentrated near the spiral slots. This indicates that the contact geometry is a key factor in determining the distribution of the magnetic field. Therefore, the influence of contact geometry on the AMF is crucial under short-circuit conditions. To facilitate the analysis of the AMF distribution on the arc center plane, a circular surface was defined at the center of the arc. For further observation, a radial straight line was drawn on this circular surface, which can directly quantify the AMF change along this path, as shown in Fig. 5. Figs. 5(a) and 5(b) show the AMF distribution contours on the arc center plane at the time of short-circuit current zero-crossing and peak, respectively, and (c) shows the AMF distribution curves along the radial straight line for these two moments.

Figure 5 shows that the magnetic field strength at the peak moment was significantly higher than that at the zero-crossing instant on the center plane of the arc. During the peak of the short-circuit current, the maximum AMF strength reached 0.128 T. In the radial direction of the arc center plane, the AMF initially increased and then slightly decreased as it approached the center, creating a highly symmetrical pattern across the center plane. When the current crossed zero, the AMF strength dropped below 40 μT, and although the spatial distribution remained centrally symmetrical, it was evident that the contact had lost its ability to actively control the arc at this stage.

In this study, the Bz distribution curve along the radial straight line on the center plane of the arc is further analyzed through Fig. 5(c), and this difference is quantitatively demonstrated: the curve is M-shaped at the peak moment, indicating that the magnetic field is highly uniform in the core region; at the zero-crossing instant, the curve is close to the baseline, and the AMF strength is almost zero, only slightly rising at the center position, which reflects the weak guiding effect of the structure itself.

3. STUDY ON THE AMF IN VACUUM INTERRUPTERS UNDER DIFFERENT PARAMETERS

3.1. Influence of Different Parameters on the Maximum AMF in Vacuum Interrupters

To systematically evaluate the influence of each parameter on the magnetic field characteristics, the sensitivity of the four core geometric parameters was studied through single-parameter sweeps. In this study, four key geometric parameters of the

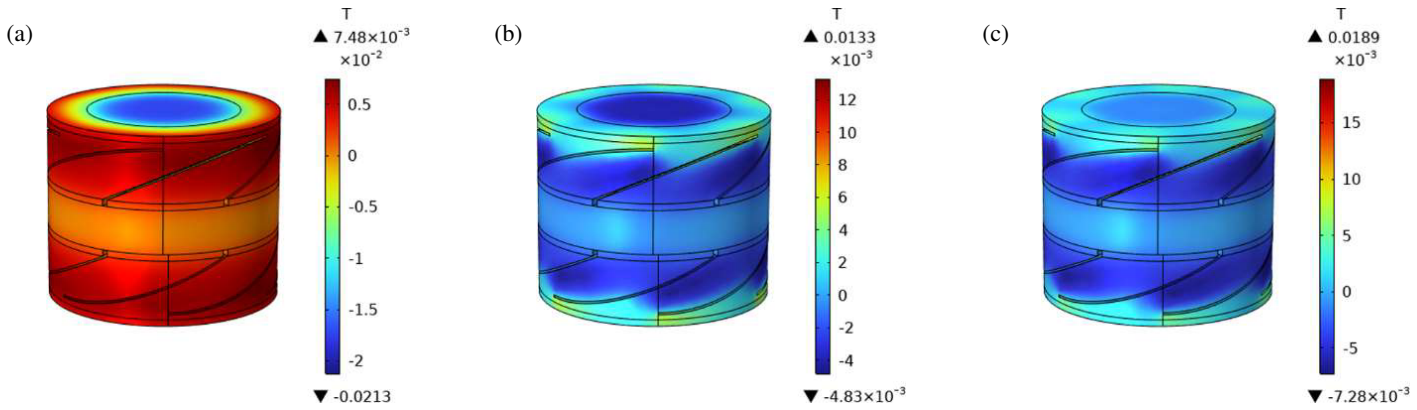

FIGURE 4. AMF distribution on contacts under short-circuit conditions at: (a) 0.5 s, (b) 1 s, (c) 2 s.

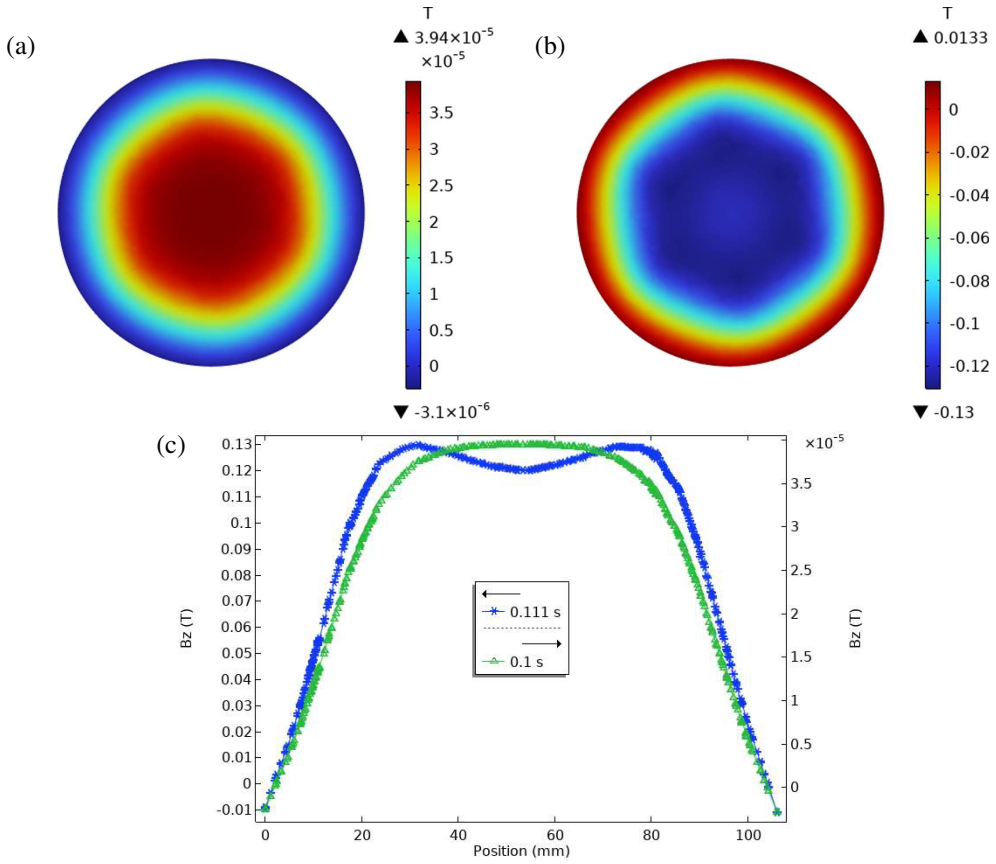

FIGURE 5. AMF distribution on the arc center plane: (a) zero-crossing current, (b) peak current, and (c) radial distribution profile.

contact system were selected: contact slotting angle α, cup finger angle β, slotting width d, and slotting length L. The angles α and β primarily affect the current flow path in the contact area, whereas the width d and length L are directly related to the size of the effective conductive region. Improper design of these four parameters can affect the magnetic field distribution and stability of the arc motion. Therefore, optimizing these parameters is essential to enhancing the AMF strength and ensuring reliable magnetic field support for the effective control of short-circuit arcs.

To focus on the most severe electromagnetic load conditions and ensure the comparability of results across parameters, all single-parameter simulations were based on the current peak instant ($t = 0.111$ s). The AMF distribution at this time best reflects the magnetic characteristics under short-circuit conditions, serving as a critical basis for the sensitivity analysis and optimization. Owing to geometric constraints, the ranges of α, β, L, and d are 18–26°, 90–110°, 10–20 mm, and 0.5–3 mm, respectively. Using the data in Table 1, these variables were independently varied and calculated, with the simulation results under short-circuit conditions shown in Fig. 6.

Figure 6 shows the individual influence of four key geometric parameters on the maximum AMF strength. As shown in Fig. 6(a), with the increase of the slotting angle α from 18° to 26°, Bz.max showed a downward trend overall. When $\alpha = 18°$, the AMF reaches a peak of 0.331 T. This is because

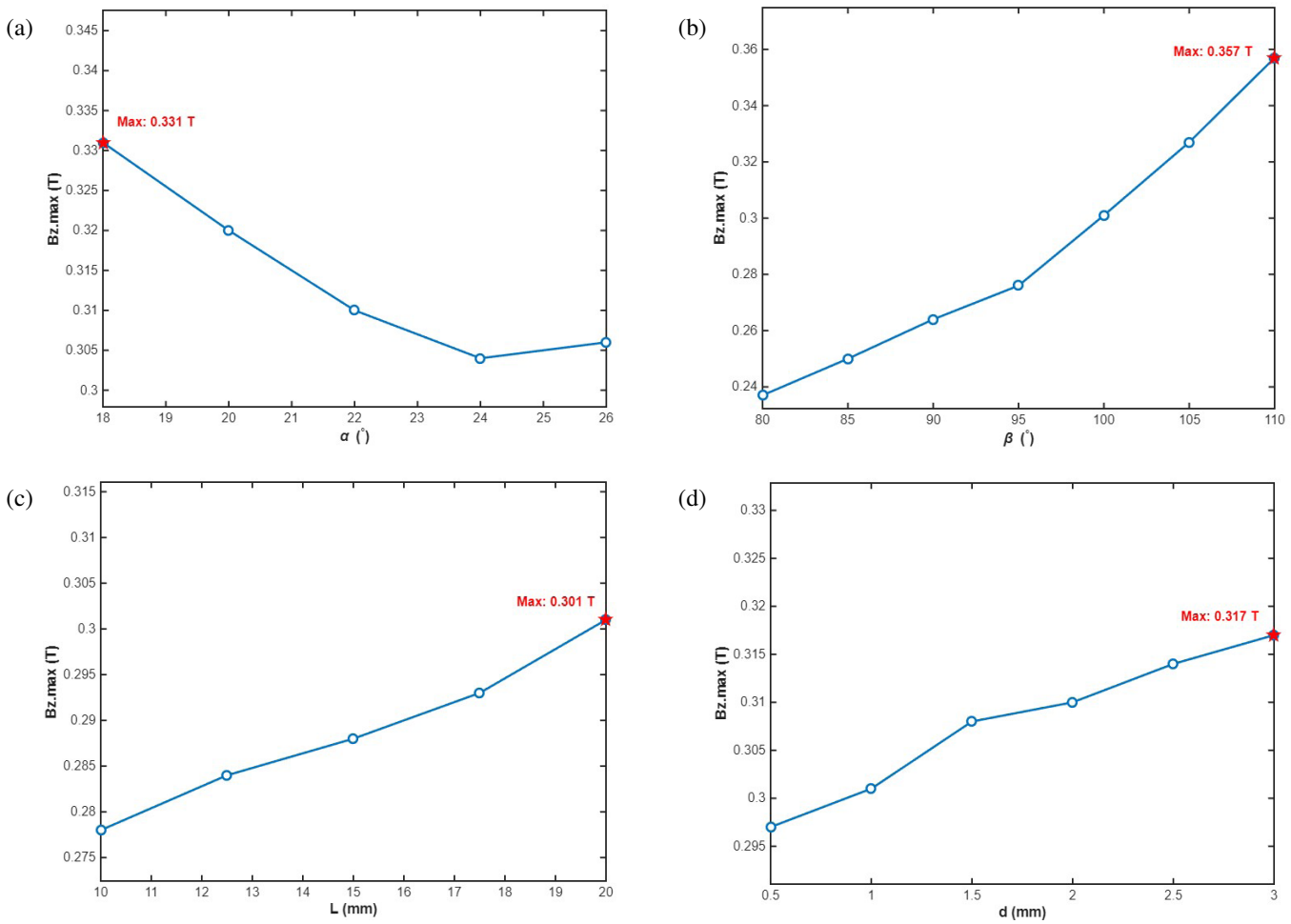

FIGURE 6. Univariate effects of four key geometric parameters on the maximum AMF strength, (a) study α, (b) study β, (c) study L, (d) study d.

a smaller slotting angle α results in a larger effective cross-sectional area for magnetic flux of the contact pad, which enhances the AMF in the central area. Furthermore, a larger α alters the shape of the current loops in the contact region. The induced eddy current paths are forced to close over a wider circumferential range, causing their reverse magnetic field components to concentrate more on the center of the arc gap, thereby partially canceling out the axial magnetic field generated by the short-circuit current excitation. In Fig. 6(b), there is a clear monotonic increasing trend between Bz.max and the contact cup finger angle β. In the process of increasing β from 80° to 110°, Bz.max increased from 0.237 T to 0.357 T, representing the largest overall change. With the increase of the β angle, this large-angle structure optimizes the reluctance distribution of the magnetic circuit, reduces magnetic leakage, and allows more magnetic flux to be concentrated in the arc region, thereby more effectively generating AMF components. In Fig. 6(c), Bz.max increases with the increase of the slotting length L of the contact finger and also shows a clear monotonic increasing trend. When L changes from 10 mm to 20 mm, Bz.max increases from 0.278 T to 0.301 T, representing a smaller overall change. Increasing the slotting length L extends the effective area of the AMF, which is conducive to increasing the magnetic field strength. Finally, in Fig. 6(d), there is a clear monotonic increasing trend between Bz.max and the slotting width d. When d increased from 0.5 to 3 mm, Bz.max increased from 0.297 to 0.317 T, a relatively small increase. The increase in the slotting width d makes the overall current distribution more uniform, which effectively promotes the AMF generation in the contact area and increases the AMF strength.

3.2. Influence of Different Parameters on the AMF at the Arc Center Plane

To further quantify the influence of these different parameters on the AMF of the arc center plane, this study selects the zero-crossing instant and current peak instant of the short-circuit current, and analyzes the AMF distribution on the arc center plane under different parameters based on the same radial path.

3.2.1. Influence of Contact Slotting Angles α on AMF Distribution

Figure 7 shows the effects of different slotting angles α on the AMF distribution on the center plane of the arc. As shown in Fig. 7(a), the corresponding AMF d variation trend is the same for different slotting angles. When α is the largest, the AMF strength is the smallest, and when α is the smallest, the AMF strength is the largest. The overall AMF strength decreased

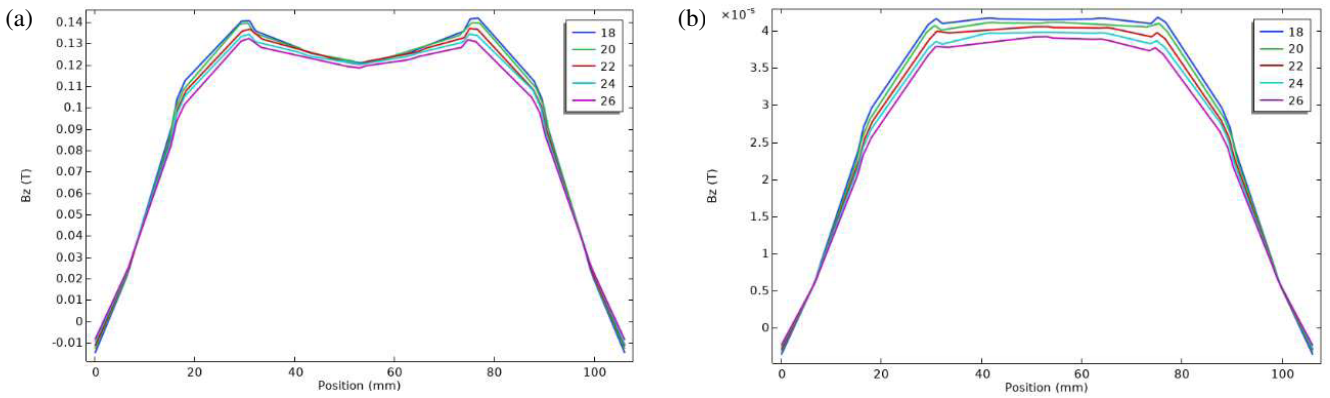

FIGURE 7. Influence of different slotting angles α, (a) study peak current, (b) study zero-crossing current.

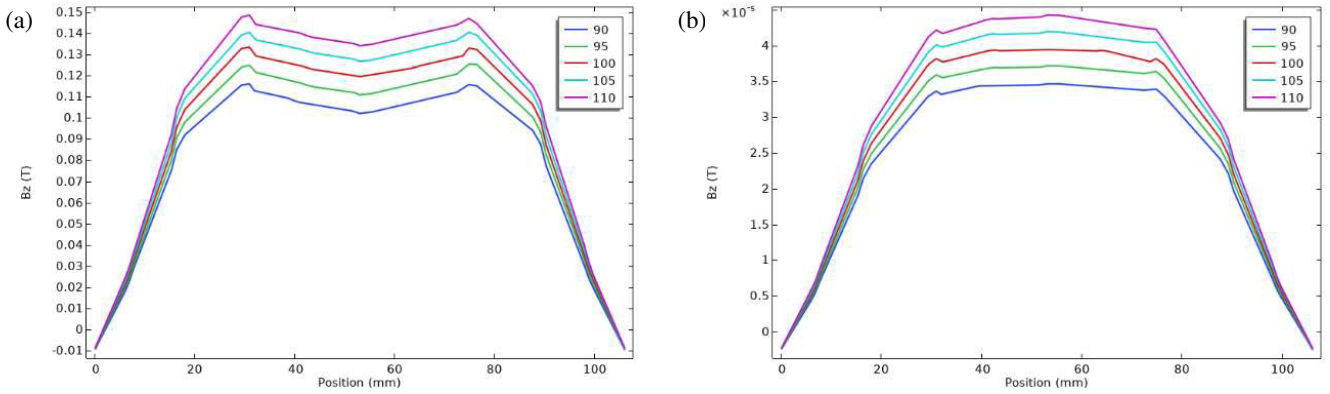

FIGURE 8. Influence of different cup finger angles β, (a) study peak current, (b) study zero-crossing current.

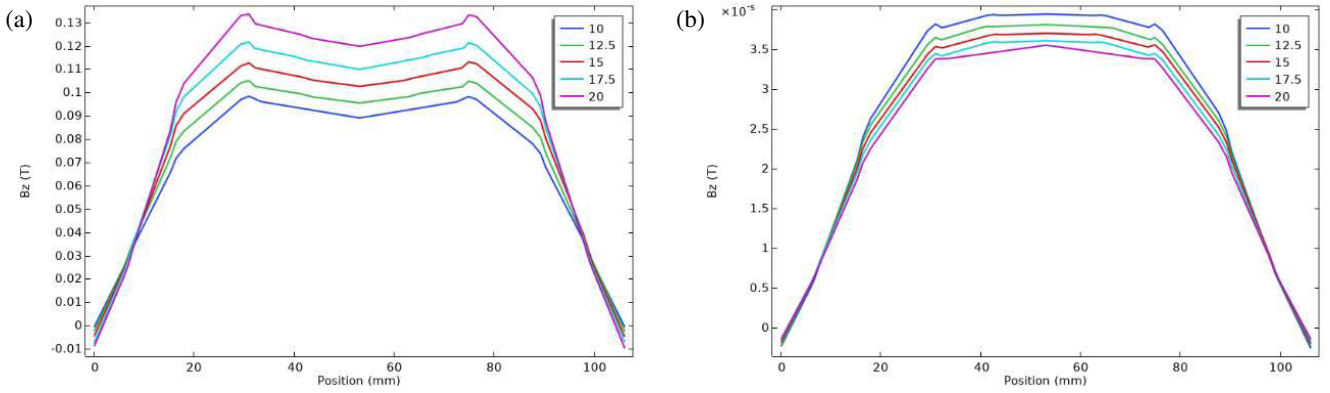

FIGURE 9. Influence of different slotting lengths L, (a) study peak current, (b) study zero-crossing current.

with the increase of α. However, the gradient of the AMF variation is small between different values of α. When the current is at its peak, the stronger the magnetic field is, the more conducive it is to a successful interruption by the interrupter. As shown in Fig. 7(b), when $\alpha = 26°$, the residual magnetic field at the zero-crossing is the smallest, and the overall residual magnetic field at the zero-crossing decreases with an increase in α.

3.2.2. Influence of Contact Cup-Finger Angle on AMF Distribution

In addition to the slotting angle α, the contact cup finger angle β is an important geometric parameter in contact systems. As shown in Fig. 8(a), the AMF variation gradient corresponding to different values of β is large, and the change trend is the same. When β is 110°, the AMF strength is the largest; when β is 90°, the AMF strength is the smallest; and the overall AMF strength increases with the increase of β. It can be seen from Fig. 8(b) that the residual magnetic field at the zero-crossing increases with an increase in β, and the change in gradient of the residual magnetic field at the zero-crossing is also large.

3.2.3. Influence of Contact Slotting Lengths L on AMF Distribution

Figure 9 shows the effect of different slotting lengths L on the AMF distribution in the arc center plane. As shown in Fig. 9(a),

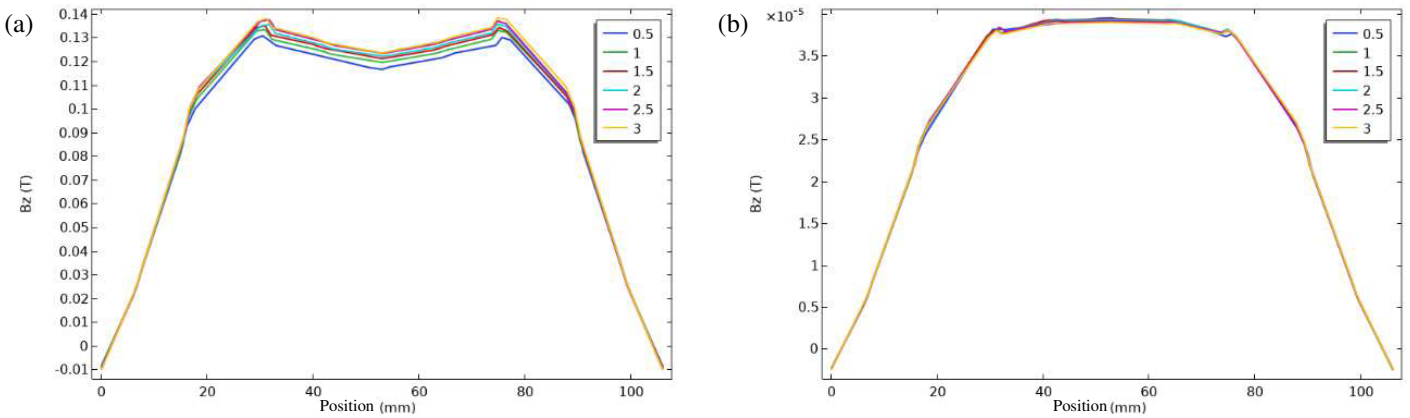

FIGURE 10. Influence of different slotting widths d, (a) study peak current, (b) study zero-crossing current.

the variation trend of the AMF corresponding to each length is the same. When L was 20 mm, the AMF was the largest, and when L was 10 mm, the AMF was the smallest. Overall, when the length L increased, the entire AMF strength also increased. The gradient of the AMF variation was relatively large between different values of L, and this gradient increased as L decreased. As shown in Fig. 9(b), the variation pattern of the residual magnetic field at the zero-crossing was diametrically opposite to that of the peak magnetic field. When L is 20 mm, the corresponding residual magnetic field at zero-crossing is the smallest; on the contrary, when L is 10 mm, the corresponding residual magnetic field is the largest, and the overall residual magnetic field at zero-crossing decreases with the increase of L. This is because the longer the slot is, the stronger the impedance effect is on the generation of eddy currents; therefore, the smaller the induced eddy current is, and the weaker the opposing magnetic field it generates. Thus, the AMF generated by external excitation is more fully established. Furthermore, when the current crossed zero, the magnetic field residue caused by the eddy current was smaller.

3.2.4. Influence of Contact Slotting Widths d on AMF Distribution

The influence of different slotting widths d on the AMF distribution on the arc center plane is illustrated in Fig. 10. The results show that the AMF variation trend is the same for different values of d: when d is the smallest, the AMF strength is the smallest, and vice versa. Furthermore, when d is 2.5 mm and 3 mm, the overall AMF variation curves are identical. As shown in Fig. 10(b), for d within the range of 0.5–3 mm, the residual magnetic field variation curves almost coincide. This indicates that the change in the slotting width d has no obvious effect on the residual magnetic field in this range.

4. ORTHOGONAL EXPERIMENTAL DESIGN AND SIMULATION RESULTS

To optimize multiple parameters, an orthogonal experimental design was used in this study. The levels of each factor were optimized and screened according to the trends observed in the single-factor tests, and the parameter ranges yielding the best AMF strength were selected to improve the experimental efficiency. The level settings for the specific parameters are listed in Table 3.

TABLE 3. Orthogonal experiment factors and levels.

Factor	Level1	Level2	Level3
α (°)	18	20	22
β (°)	100	105	110
L (mm)	15	17.5	20
d (mm)	2	2.5	3

To significantly reduce the computational cost and time, this study employed an $L_9(3^4)$ orthogonal array comprising nine simulation runs, as shown in Table 4. The orthogonal table reduced the 81 (3^4) of the whole factor test to 9 while ensuring the accuracy of the analysis. In addition, to account for the boundary effects near the optimal combination, 10 additional simulation runs were added for extrapolation verification. All the simulation cases maintained identical boundary conditions.

Table 4 shows that the Bz.max distribution of the 9 orthogonal runs ranges from 0.317 T to 0.380 T. The maximum AMF occurs in Run 3 ($\alpha = 18°$, $\beta = 110°$, $L = 20$ mm, $d = 3$ mm), and the minimum value occurs in Run 1 ($\alpha = 18°$, $\beta = 100°$, $L = 15$ mm, $d = 2$ mm). The range is 0.063 T, indicating that the combination of parameters has a significant effect on the AMF strength of the vacuum interrupter. The AMF strength of

TABLE 4. Orthogonal experiment scheme.

No.	α (°)	β (°)	L (mm)	d (mm)	Bz.max (T)
1	18	100	15	2	0.317
2	18	105	17.5	2.5	0.343
3	18	110	20	3	0.380
4	20	100	17.5	3	0.327
5	20	105	20	2	0.344
6	20	110	15	2.5	0.365
7	22	100	20	2.5	0.321
8	22	105	15	3	0.342
9	22	110	17.5	2	0.362
10	18	111	20	3.2	0.372

Run 10 is 0.372 T, which is lower than that of Run 3. This indicates that the magnetic field strength does not increase when $\beta > 110°$ or $d > 3$ mm, suggesting the existence of an optimal boundary. Moreover, when $\beta = 100°$, the AMF is generally low, preliminarily suggesting that β is the most critical factor among the four.

5. RSM ANALYSIS

5.1. RSM Experimental Design

To further explore the nonlinear effects of each structural parameter on the AMF field of the vacuum interrupter and the interactions among the four parameters, an RSM was conducted using the BBD method, which was built upon the orthogonal test optimization. The optimal parameter levels obtained from the previous orthogonal test served as the central points, and the factor levels for each parameter are listed in Table 5.

TABLE 5. Level coding table for the RSM.

Factor	Level 1 (−1)	Level 2 (0)	Level 3 (1)
α (°)	18	19	20
β (°)	105	108	111
L (mm)	16	18	20
d (mm)	2.4	2.8	3.2

Based on the principles of BBD, a total of 29 experimental runs were arranged. Table 6 presents a selected subset of the experimental scheme and the corresponding simulated Bz.max. Notably, the design included five replicate runs at the center point to evaluate the pure error.

TABLE 6. RSM experimental scheme and results.

α (°)	β (°)	L (mm)	d (mm)	Bz.max (T)
18	105	18	2.8	0.351
18	111	18	2.8	0.388
20	108	16	2.8	0.363
18	108	20	2.8	0.373
19	111	18	2.4	0.372
19	108	20	3.2	0.370

Subsequently, MATLAB was used to perform a second-order polynomial regression fit on the experimental data from the response surface table. To evaluate the goodness of fit and prediction reliability of the quadratic polynomial regression model and to provide a comparative benchmark, both the RSM model and a Kriging surrogate model were constructed and assessed. The key statistical indicators are summarized in Table 7.

The analysis of variance results show that the coefficient of determination R^2 is 0.8504. It indicates that the model accounts for approximately 85% of the total data variation. The gap between R^2 and $Adj\ R^2 = 0.7007$ reflects the presence of some statistically less significant terms within the 15-term quadratic polynomial, rather than overfitting. The *RMSE* of the RSM model is 4.04×10^{-3} T, with a max relative prediction error

TABLE 7. RSM and Kriging surrogate model performance.

Indicator	RSM	Kriging
R^2	0.8504	0.9999
$Adj\ R^2$	0.7007	0.9998
RMSE	4.04e-3	1.27e-4
Max relative error (%)	2.97	0.10
Average relative error (%)	0.78	0.03

of 2.97% and an average relative error of 0.78%, indicating an acceptable prediction accuracy within the design space.

To further validate the quality of the simulation dataset, a Kriging surrogate model was also constructed using the same 29 design points. This Kriging model achieved an R^2 of 0.9999 and an *RMSE* of 1.27×10^{-4} T, with a maximum relative error of only 0.10%, confirming that the underlying simulation data possesses a high degree of consistency. Collectively, these two models demonstrate the reliability of the optimization results presented in this study.

5.2. RSM Analysis and Parameter Interaction Effects

To visually show the influence of various factors and their interactions on Bz.max, this paper draws a three-dimensional RSM map of key factors. Fig. 11 presents the 3D RSM plots for the interactions between β and L (left), and β and d (right). From the left plot, it is evident that there is a significant interaction between β and L. When β is small, Bz.max increases monotonically with the increase in slot length L; however, as β gradually increases to higher levels, the response surface exhibits a curved trend. When L continues to increase to larger values, its enhancement effect on the maximum AMF Bz.max diminishes and even shows a downward trend. This indicates that under conditions of large cup-finger rotation angles, an excessively long contact slot length leads to magnetic circuit saturation and increased magnetic leakage, thereby producing a negative effect that offsets the gains achieved by increasing the L. From the right plot, it is also clear that the interaction between β and d is highly significant. In the case of large β angles, variations in d have a drastic impact on Bz.max. The RSM predicts a peak region near $\beta = 111°$, suggesting that the optimal value for d may not be at the boundary maximum but rather located within an intermediate range. Based on this RSM, global optimization predicted a theoretical optimal parameter combination: $\alpha = 18°$, $\beta = 111°$, $L = 20$ mm, $d = 3.2$ mm. However, the simulation results of the 10th set of orthogonal tests show that the AMF peak is 0.372 T, which is not the maximum AMF. Considering that quadratic polynomials have extrapolation limitations in the edge region of the parameter value, therefore, to avoid this risk and find the true optimal solution, a more detailed simulation test is carried out in the area near the theoretical optimal solution in order to avoid this risk and find the true optimal solution. Based on $\alpha = 18°$ and $\beta = 111°$, L and d were moderately changed to explore the global optimum. The detailed test results are presented in Table 8.

As shown in Table 8, the AMF peaks of the other three configurations exceeded those of the boundary combination. In the

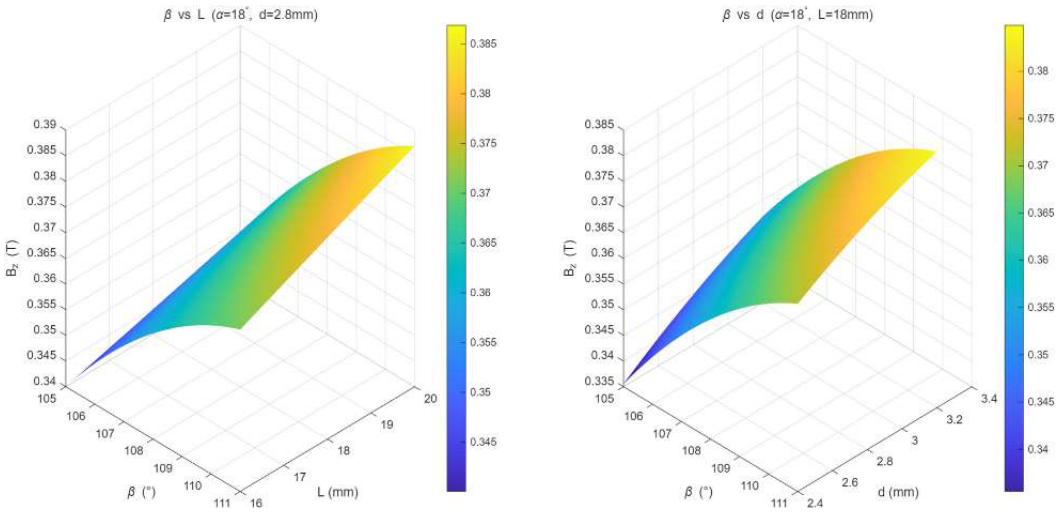

FIGURE 11. RSM diagram of key factor interactions.

TABLE 8. Results of parameter refinement experiments in the boundary region.

No.	α (°)	β (°)	L (mm)	d (mm)	Bz.max (T)
1	18	111	20	3.2	0.372
2	18	111	20	3.1	0.378
3	18	111	20	2.8	0.384
4	18	111	18	3.2	0.364
5	18	111	18	3.1	0.371
6	18	111	18	2.8	0.388

axial view, L remained unchanged, and Bz.max increased as d decreased. When L was reduced from 20 to 18 mm and Bz.max increased to 0.388 T. This indicates that appropriately shortening the slotting length L optimizes the AMF distribution and enhances the field strength. Based on this analysis, group 6 not only avoided the unreliable boundary region but also yielded a superior AMF peak. Therefore, by combining the RSM with the boundary refinement verification, Group 6 was selected as the final optimal design.

To evaluate whether the optimized design would negatively impact the arc recovery phase, the residual axial magnetic flux density at current zero was extracted from the existing transient simulation results for both the baseline and optimized designs, as summarized in Table 9. The optimized design increased Bz.max by 28.9%, while the ratio of the residual axial magnetic flux density to Bz.max remained nearly constant. This indicates that the proposed optimization method does not introduce a high residual magnetic field at the current zero.

TABLE 9. Peak and residual AMF comparison for baseline and optimized designs.

Design	max (T)	residual (T)	residual /max
Baseline	0.301	7.40×10^{-5}	0.0246%
Optimized	0.388	9.49×10^{-5}	0.0245%

6. CONCLUSION

In this paper, a three-dimensional transient electromagnetic field simulation model considering the measured short-circuit current excitation is established for a vacuum interrupter, and the influence of four key geometric parameters on the AMF field distribution of contact slotting angle α, cup finger angle β, slotting length L, and slotting width d is systematically studied. Through univariate analysis, orthogonal test screening, global optimization of response surface method (BBD), and boundary refinement verification, the multi-parameter co-optimization of contact structure is realized. The main conclusions are as follows:

(1) First, the results of single-parameter analysis show that the influences of these four parameters on the AMF field and the remaining magnetic field are different. Among them, β and L are the main factors affecting AMF, and the AMF increases significantly with the increase of β and L. The slotting angle α negatively correlated with the AMF, which decreases with the increase of α, but the change gradient is slow. The slotting width d is saturated once it exceeds 2.5 mm, and the AMF lift is not large, remaining nearly constant.

(2) Second, in view of the complexity of multi-parameter optimization, a phased optimization method of orthogonal test preliminary screening, RSM analysis, and boundary refinement verification is adopted. It is found that the influence of the angle β of the cup finger on AMF is the most critical, and the interaction between parameters is discussed through the further analysis of the RSM quadratic regression model.

(3) Finally, the deviation of the theoretical optimal value is corrected by using boundary verification. The optimal combination of structural parameters obtained through the whole phased optimization is: slotting angle $\alpha = 18°$, cup finger angle $\beta = 111°$, slotting length $L = 18$ mm, slotting width $d = 2.8$ mm, under this optimal working condition, the maximum AMF strength of the vacuum interrupter at the moment of 57.7 kA short-circuit peak current reaching 0.388 T, representing a 28.9% increase compared to the benchmark model's peak AMF of 0.301 T.

The phased collaborative optimization method proposed in this study reveals the influence of complex contact structure parameters on the AMF. The study provides a clear theoretical basis for the refined design of high-performance vacuum interrupters. The optimized contact structure significantly improved the axial magnetic flux density, enhanced the breaking capacity and arc diffusion efficiency at high currents, and offers valuable guidance for the development of a new generation of compact, large-capacity, long-life, and environmentally friendly vacuum circuit breakers.

ACKNOWLEDGEMENT

This research was funded by the National Key R&D Program of China, grant number "2022YFB2403600".

REFERENCES

[1] Hu, X., H. Li, H. Li, Z. Song, X. Gao, and J. Li, "Design and test of magnetic shielding for vacuum circuit breaker of CRAFT quench protection system," *IEEE Transactions on Plasma Science*, Vol. 51, No. 10, 3178–3187, Oct. 2023.

[2] Chen, H., X. Liu, L. Li, Y. Liu, Y. Zhang, and Y. Huang, "Analysis of dynamic arc parameters for vacuum circuit breaker under short-circuit current breaking," *IEEE Transactions on Applied Superconductivity*, Vol. 29, No. 2, 1–5, Mar. 2019.

[3] Han, J.-R., Z.-H. Dou, T.-A. Zhang, and W. An, "Review of the recent Chinese research on the electrical properties of CuCr contacts for vacuum interrupters," *Journal of Materials Research and Technology*, Vol. 25, 1585–1598, 2023.

[4] Liu, X. M., Y. Y. Zhao, H. Chen, and F. Y. Wen, "Analysis of influencing factors of arc motion characteristics of DC transverse magnetic vacuum interrupter," *Chinese Journal of Vacuum Science and Technology*, Vol. 45, No. 3, 197–204, 2025.

[5] Sevillano, J. F., L. Combarro, A. Irizar, I. P. Gilbert, J. Izagirre, and F. Arizti, "A contactless pirani approach for vacuum monitoring in vacuum circuit breakers," *IEEE Sensors Journal*, Vol. 23, No. 2, 1592–1600, Jan. 2023.

[6] Götte, N., T. Krampert, and P. G. Nikolic, "Series connection of gas and vacuum circuit breakers as a hybrid circuit breaker in high-voltage applications," *IEEE Transactions on Plasma Science*, Vol. 48, No. 7, 2577–2584, Jul. 2020.

[7] Ide, N., O. Tanaka, S. Yanabu, S. Kaneko, S. Okabe, and Y. Matsui, "Interruption characteristics of double-break vacuum circuit breakers," *IEEE Transactions on Dielectrics and Electrical Insulation*, Vol. 15, No. 4, 1065–1072, Aug. 2008.

[8] Zhang, H., M. Liao, Y. Fu, Z. Chen, H. Dong, and J. Zou, "Effect of arcing time on voltage distribution of double-break vacuum circuit breaker during the transient recovery voltage rising phase," *IEEE Transactions on Plasma Science*, Vol. 49, No. 4, 1357–1362, Apr. 2021.

[9] Huang, D., G. Wu, and J. Ruan, "Study on static and dynamic voltage distribution characteristics and voltage sharing design of a 126-kv modular triple-break vacuum circuit breaker," *IEEE Transactions on Plasma Science*, Vol. 43, No. 8, 2694–2702, Aug. 2015.

[10] Tian, Y., J. Xu, Y. Deng, Y. Wang, E. Dong, and J. Zou, "Development and tests of ZW-126/D2000-40 vacuum circuit breakers with controlled switching technology," *CSEE Journal of Power and Energy Systems*, Vol. 8, No. 1, 249–257, Jan. 2022.

[11] Razi-Kazemi, A. A., M. R. Fallah, and M. Rostami, "A hybrid-approach for realtime assessment of the pressure and erosion in vacuum circuit breakers," *IEEE Transactions on Dielectrics and Electrical Insulation*, Vol. 27, No. 6, 2087–2094, Dec. 2020.

[12] Stoczko, S., M. Szewczyk, W. Chmielak, R. Szreder, and Z. Pochanke, "Measurements of breakdown voltage characteristics of medium voltage vacuum circuit breaker after current interruption," *IEEE Transactions on Power Delivery*, Vol. 40, No. 2, 1214–1222, Apr. 2025.

[13] Wang, D., L. Wang, Z. Wang, Y. Huang, R. Zhang, and S. Jia, "2-D particle simulation on the influence of transverse magnetic field on the plasma decay in postarc stage of vacuum circuit breakers," *IEEE Transactions on Plasma Science*, Vol. 48, No. 11, 3975–3981, Nov. 2020.

[14] Han, X., F. Yang, H. Chen, Y. Bai, Z. Gu, J. Sun, Y. Wu, W. Yang, and M. Rong, "Parallel current-sharing characteristics of vacuum multi-breakers for large-capacity generator circuit breakers," *IEEE Transactions on Power Delivery*, Vol. 39, No. 2, 1162–1173, Apr. 2024.

[15] Mo, Y., Z. Shi, S. Jia, and J. Li, "Experimental investigation on the postarc current in vacuum circuit breakers and the influence of arcing memory effect," *IEEE Transactions on Plasma Science*, Vol. 47, No. 8, 3508–3515, Aug. 2019.

[16] Li, D. H., "Research on electromagnetic and mechanical characteristics of cup-shaped axial magnetic field contacts in vacuum interrupters," Dalian Jiaotong University, Dalian, China, 2022.

[17] Xu, R., J. Wang, Y. Zhao, and P. Yan, "Characteristics of electromagnetic field and arc motion in vacuum interrupter with longitudinal magnetic field contacts," *High Power Laser and Particle Beams*, Vol. 24, No. 4, 855–858, 2012.

[18] Ding, C., Z. W. Jia, Z. Yuan, and J. N. Liu, "Optimization design of iron-core axial magnetic field contacts in vacuum interrupters based on SSA-SVR and NSGA-III," *High Voltage Apparatus*, 1–13, 2026.

[19] Dong, H. J., M. Y. Si, Y. J. Guo, C. X. Li, and F. Guo, "Influence of contact plate structure on magnetic field strength of a new type of cup-shaped axial magnetic field vacuum interrupter with iron core," *Transactions of China Electrotechnical Society*, Vol. 33, No. 11, 2448–2455, 2018.

[20] Chen, T. D., "Optimization of contact structure for cup-shaped axial magnetic field vacuum interrupter based on artificial current zero breaking," Huazhong University of Science and Technology, Wuhan, China, 2019.

[21] Ding, C., J. Li, Z. Yuan, L. X. Chen, and L. M. Liu, "Structural optimization design of cup-shaped longitudinal magnetic contact based on NSGA-II and BP neural network," *Transactions of China Electrotechnical Society*, Vol. 37, No. 23, 6074–6082, 2022.

[22] Wang, Z. H., H. M. Li, J. H. Wang, Z. Y. Liu, Q. Wang, L. P. Yan, and Y. L. Zhang, "Analysis and optimization of magnetic field characteristics for vacuum interrupter with horseshoe-shaped axial magnetic field contacts based on response surface method," *High Voltage Apparatus*, Vol. 53, No. 3, 90–96, 2017.

[23] Ding, C., Z. L. Wang, Z. Yuan, and J. Li, "Structural optimization design of vacuum interrupter contact based on multi-objective grey wolf optimization algorithm and rbf neural network," *High Voltage Engineering*, Vol. 50, No. 2, 545–552, 2024.

[24] Yang, J. W., T. Tan, S. X. Xiu, S. L. Tan, H. Y. Luo, and Z. Q. Tian, "Magnetic field characteristics of cup-shaped axial magnetic field contact under the condition of large contact gap," *High Voltage Engineering*, Vol. 49, No. 7, 3125–3133, 2023.

[25] Wang, W. C., "Research on structural optimization design of vacuum interrupter based on electromagnetic field simulation analysis," Shandong University of Technology, Zibo, China, 2022.

[26] Si, M. Y., "Simulation study on influence of structure on electromagnetic field distribution in new type vacuum interrupter," Dalian Jiaotong University, Dalian, China, 2018.

[27] Wen, C. Y., "Simulation study on magnetic field and temperature field of vacuum interrupter with new composite contacts," Dalian Jiaotong University, Dalian, China, 2022.

[28] Ding, C., J. Li, Z. Yuan, and Z. L. Wang, "Optimal design of transverse magnetic-axial magnetic contact structure with iron core," *Transactions of China Electrotechnical Society*, Vol. 39, No. 11, 3499–3509, 2024.

[29] Chen, H., X. Liu, L. Li, Y. Liu, Y. Zhang, and Y. Huang, "Analysis of dynamic arc parameters for vacuum circuit breaker under short-circuit current breaking," in *2018 IEEE International Conference on Applied Superconductivity and Electromagnetic Devices (ASEMD)*, 1–2, Tianjin, China, 2018.